Respiratory Physiology & Neurobiology 260 (2019) 82–94

Contents lists available at ScienceDirect

Respiratory Physiology & Neurobiology

journal homepage: www.elsevier.com/locate/resphysiol

Mice-to-men comparison of inhaled drug-aerosol deposition and clearance

Arun V. Kolanjiyil[a], Clement Kleinstreuer[a,b,*], Nicole C. Kleinstreuer[c], Wellington Pham[d], Ruxana T. Sadikot[e,f]

[a] *Department of Mechanical & Aerospace Engineering, North Carolina State University, Raleigh, NC 27695-7910, United States*
[b] *Joint UNC-NCSU Department of Biomedical Engineering, North Carolina State University, Raleigh, NC 27695-7910, United States*
[c] *National Institute of Environmental Health Sciences (NIEHS), National Toxicology Program Interagency Center for Evaluation of Alternative Toxicological, Methods (NICEATM), United States*
[d] *Department of Radiology and Radiological Sciences, Vanderbilt University, Institute of Imaging Science, United States*
[e] *Division of Pulmonary, Allergy and Critical Care Medicine, Emory University, School of Medicine, United States*
[f] *Department of Veterans Affairs, Atlanta VAMC, United States*

ARTICLE INFO

Keywords:
Lung deposition
Mouse lung model
Human lung model
Dose extrapolation
Pharmacokinetics

ABSTRACT

Part of the effective prediction of the pharmacokinetics of drugs (or toxic particles) requires extrapolation of experimental data sets from animal studies to humans. As the respiratory tracts of rodents and humans are anatomically very different, there is a need to study airflow and drug-aerosol deposition patterns in lung airways of these laboratory animals and compare them to those of human lungs. As a first step, interspecies computational comparison modeling of inhaled nano-to-micron size drugs ($50\,\text{nm} < d < 15\,\mu\text{m}$) was performed using mouse and human upper airway models under realistic breathing conditions. Critical species-specific differences in lung physiology of the upper airways and subsequently in local drug deposition were simulated and analyzed. In addition, a hybrid modeling methodology, combining Computational Fluid-Particle Dynamics (CF-PD) simulations with deterministic lung deposition models, was developed and predicted total and regional drug-aerosol depositions in lung airways of both mouse and man were compared, accounting for the geometric, kinematic and dynamic differences. Interestingly, our results indicate that the *total* particle deposition fractions, especially for submicron particles, are comparable in rodent and human respiratory models for corresponding breathing conditions. However, care must be taken when extrapolating a given dosage as considerable differences were noted in the *regional* particle deposition pattern. Combined with the deposition model, the particle retention and clearance kinetics of deposited nanoparticles indicates that the clearance rate from the mouse lung is higher than that in the human lung. In summary, the presented computer simulation models provide detailed fluid-particle dynamics results for upper lung airways of representative human and mouse models with a comparative analysis of particle lung deposition data, including a novel mice-to-men correlation as well as a particle-clearance analysis both useful for pharmacokinetic and toxicokinetic studies.

1. Introduction

Respiratory drug delivery is becoming an increasingly popular way of administering therapeutic agents. Targeted delivery to the desired lung sites can provide very effective treatment options, including: (i) instantaneous onset of action; (ii) minimal side effects; and (iii) maximal use of drugs at the affected area (Kleinstreuer et al., 2014; Kolanjiyil et al., 2016). In addition, many systemic pathogenic conditions can be treated via rapid absorption of inhaled drugs through the large surface area of the alveolar lung region into the blood circulation towards affected organs (Kolanjiyil and Kleinstreuer, 2013). The large surface area of the lungs and the minimal barriers impeding access to the lung periphery make this organ a suitable portal for a variety of therapeutic interventions. The blood barrier between the alveolar space and the pulmonary capillaries is very thin, allowing for rapid gas exchange. Alveoli are small and there are approximately 300 million of them in each lung. Although alveoli are tiny structures, they have a very large surface area ($\sim 100\,\text{m}^2$) for performing efficient gas exchange and facilitating direct drug delivery (Sadikot and Rubinstein, 2009; Sadikot, 2012). Among the various drug delivery systems considered for pulmonary application, *nanoparticles* demonstrate several advantages for the treatment of respiratory diseases, like prolonged drug release, cell-specific targeted drug delivery or modified biological distribution of drugs, both at the cellular and organ level (Sadikot,

---

* Corresponding author at: Department of Mechanical & Aerospace Engineering, North Carolina State University, Raleigh, NC 27695-7910, United States.
E-mail address: ck@ncsu.edu (C. Kleinstreuer).

https://doi.org/10.1016/j.resp.2018.11.003
Received 6 July 2018; Received in revised form 7 November 2018; Accepted 10 November 2018

2014). Finally, yet importantly, respiratory delivery is ideal for drugs where degradation *via* first-pass metabolism becomes an issue.

Animal models are surrogates for humans when testing new drugs (Phalen and Mendez, 2009; Phalen et al., 2010). Effective prediction of human pharmacokinetics of new drugs requires extrapolation of experimental results from animal studies to humans. Most commonly used surrogate laboratory animals to test the effects of inhaled toxic/therapeutic aerosols are mice and rats. Therefore, it is imperative to translate the lung-aerosol dynamics of laboratory animals to humans to ensure realistic clinical predictions, as the lung structure and the inhalation characteristics of rodents and humans are very different (Minard et al., 2006; Namati, 2009; Thiesse et al., 2010). Toxicological and pharmacological inhalation studies in both laboratory animals and humans showed that the particle dose is dependent on the species type, inhalation method, exposure technology, and inhalation device (Wolff, 2015). Interspecies differences in the lung geometry can lead to large variations in particle deposition pattern and hence the site-specific dosage (Menache et al., 1995). Furthermore, the differences in particle deposition may result in large variation of particle retention, clearance and translocation from the deposited sites (Hsieh et al., 1999). Particle retention and clearance are of major concern in inhalation toxicology and pharmacology, especially for the treatment of lung diseases and understanding the impact of air pollutants and inhaled toxicants (Geiser and Kreyling, 2010). Investigations related to the deposition and removal of inhaled nanomaterial is of great importance because accumulation and retention of, e.g., toxic nanoparticles can result in serious lung diseases (Kolanjiyil and Kleinstreuer, 2013). In the case of multifunctional nanoparticles with polymeric nanostructures used for disease detection, imaging and drug targeting, a thorough knowledge of such nanodrugs, ie, their formulation, delivery and uptake are crucial as well. Hence, an interspecies comparison analysis focusing on local lung deposition, retention and clearance of inhaled aerosols is vital to inhalation dosage extrapolation and human-relevant predictions for both toxicological and pharmacological applications (Jarabek et al., 2005).

In order to evaluate treatment options of various diseases, the mouse lung has become a routinely used model to mimic different pathological conditions (Sadikot and Rubinstein, 2009; Sadikot, 2012). There are significant variations in mouse lung structure as compared to the human lung. Mouse lung airway bifurcations are asymmetric or monopodial in nature while the human counterparts are largely symmetrical (Winkler-Heil and Hofmann, 2016). Typically, the nasal and upper lung airway geometries of the mouse lung are extracted from high-resolution images. These analyses have revealed that the structure of the mouse nasopharyngeal region is highly complex when compared to a human nasal region. Currently, quantitative morphometric lung measurements are available only for the mouse tracheobronchial airways from lung-cast recordings (Oldham and Robinson, 2007; Oldham et al., 2009; Madl et al., 2010). In a recent report, high-resolution micro-computed tomography of the mouse acinar lung structure (Vasilescu et al., 2012) indicated that most rodents lack respiratory or terminal lung airways. While basic human lung structures has been analyzed to a certain degree, using imaging technology (Lin et al., 2009) as well as lung-cast studies (Weibel, 1963). However, due to the limited resolution of the CT images and the long processing time, detailed lung anatomical mapping is not possible except for few upper bronchial airways (Lin et al., 2009). Clearly, as the lung structures of rodents and humans are different, accurate extrapolation of fluid-particle dynamics in lung-airways of these laboratory animals to humans must account for those differences. Additionally, mice are obligated nose-only breathers, while in humans inhalable pharmaceutical drugs can be delivered via nasal or oral inhalation routes. In addition, different mechanisms are usually employed to generate/administer drug aerosols to mice and humans. Hence, extrapolation of mice inhaled exposure concentrations to humans first requires consideration of the difference in nasal and nasal/oral preferred inhalation modes (Asgharian et al., 2014).

Accurate cross-species extrapolation requires detailed animal and human total and regional lung drug deposition results (Jarabek et al., 2005). They may be obtainable via modeling and simulation where total as well as regional drug-deposition concentrations can be realistically and accurately predicted (Kleinstreuer and Zhang, 2010; Kolanjiyil and Kleinstreuer, 2017). Until recently, modeling of particle deposition in rodent lung airways still relied on reduced dimensional models or focused on only a small part of the whole lung (Asgharian et al., 2014; Oakes et al., 2015) and only limited number of studies have focused on mouse-lung deposition (Oldham and Robinson, 2007; Oldham et al., 2009; Madl et al., 2010; Moss and Oldham, 2011; Asgharian et al., 2014; Winkler-Heil and Hofmann, 2016). In addition, only limited information is available regarding particle retention and clearance in mouse lungs and most of these studies are focused on micron particles (Hsieh et al., 1999; Sakoda et al., 2012). The emergence of 3-D computational fluid-particle dynamics (CF-PD) techniques produced a significant improvement in comparative studies of airflow and particle transport in typical rat and human nasal airways (Minard et al., 2006; Corley et al., 2012; Shang et al., 2015; Xi et al., 2016). To our knowledge high-resolution rodent lung models capturing distal lung airways are limited and the currently published extensive lung models are mostly for rats. Corley and his group have developed detailed models for rats; however, simulations in a detailed mouse lung model, which is considerably smaller in size compared to a rat lung, has yet to be conducted (Corley et al., 2012). Taking advantage of CF-PD techniques, we examined and compared the airflow and particle transport in mouse versus human, employing upper airway lung models developed based on imaging portals and lung morphometric measurements reported in the literature. Furthermore, combining the CF-PD results with a deterministic lung deposition model, we estimated the total and regional lung deposition and compared the retention and clearance kinetics of the deposited nanomaterials between species. Overall, this methodology will enable extrapolation of drug-aerosol transport and deposition analysis from mice to men.

2. Particle deposition in the mouse and human upper lung airways

We examined and compared the airflow and particle transport in representative mouse versus human upper lung airways using CF-PD. The lung models employed were developed based on imaging portals and lung morphometric measurements.

2.1. Three-dimensional upper airway models

As mentioned, the computational models of the mouse and human nasal passages were derived from CT images. The mouse and human lung upper airway 3-D models are shown in Fig. 1, where the gravitational vector is acting in the negative z-direction. The mouse and human nasal models include the left and right nostrils, nasal passages and the nasopharyngeal duct. The detailed information regarding the human nasal model reconstruction and geometric development are provided in Shi et al. (2007) and Calmet et al. (2018). The mouse extrathoracic model was truncated after the larynx and an in-house mouse upper airway model was attached. The morphometric measurements from Namati (2009) and Thiesse et al. (2010) were used to develop the mouse upper lung airways. From the high-resolution image and the morphological measurements of the upper tracheobronchial airways in these studies, we developed a 3-D rendered upper airway tree, capturing airways from the trachea to generation 3. The outlets were extended to reduce outlet and downstream effects, such that the velocity was normal to the outlet planes. It should be noted that the particle deposition results were only recorded in the realistic geometry, i.e., before the extensions. Among the different strains of the laboratory mice investigated (Thiesse et al., 2010), the typically used BALB/c mouse strain was selected in this study. The tracheobronchial airway

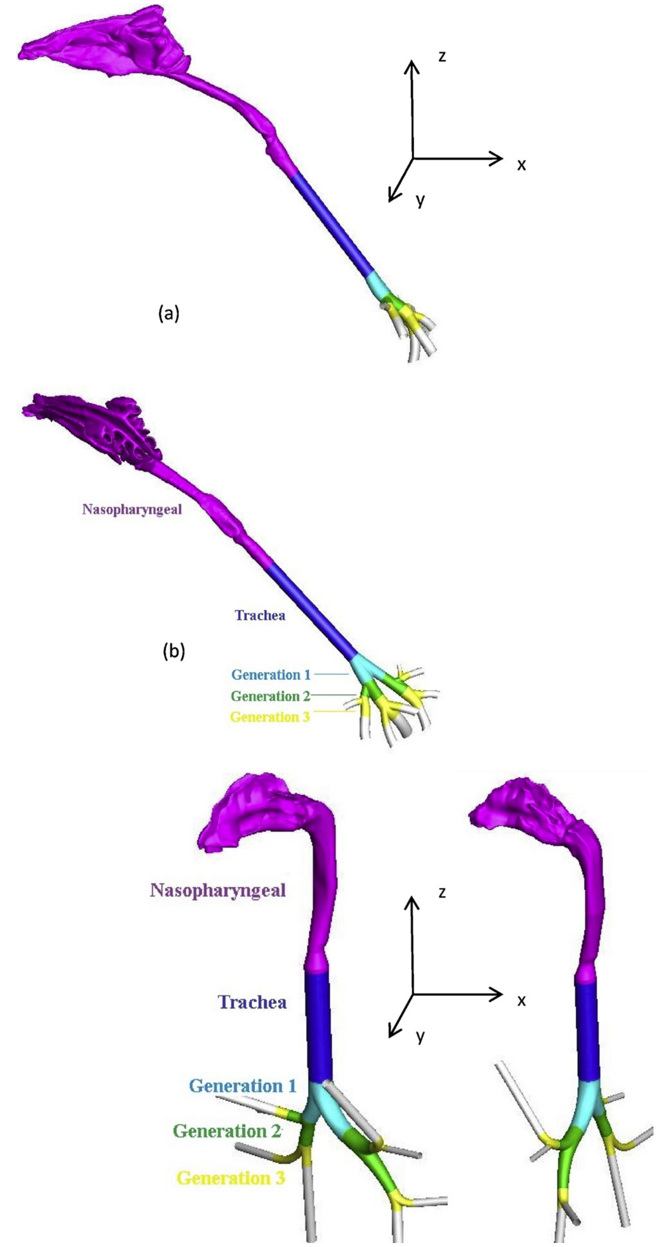

Fig. 1. Views of complete nasal-upper airway models: (a) mouse and (b) human.

model was scaled to match the dimensions of the typical mouse-lung model reported by Oldham and Robinson (2007) (see supplementary materials). Fig. 1b depicts the 3-D rendered human upper tracheobronchial airway model, while details regarding the model dimensions are reported in Li et al. (2007). Again, the outlets were extended to reduce outlet and downstream effects, such that the velocity was normal to the outlet planes. The nasopharyngeal models were scaled so that the nasopharyngeal outlet diameter matched the tracheal inlet diameter (see supplementary materials).

2.2. CF-PD model input and boundary conditions

The airway geometries were meshed using Ansys ICEM-CFD, employing unstructured tetrahedral elements with three prism layers near the wall surface. Prism layers were added to accurately capture the near-wall particle dynamics. A mesh convergence study was performed for the mouse and human models to increase the accuracy of the results and optimize the computational cost and time. The model was considered to be grid-independent when the changes in total particle deposition results were less than 2%. After the mesh-independence study, the mouse model featured 7.3 million elements while the human model had 8.2 million elements.

Table 1
Human and mouse breathing patterns.

	Human		Mouse (DeLorme and Moss, 2002)	
Condition	Rest	Light exertion	Rest	Light exertion
Mass flowrate (L/min)	15	30	66e-3	125e-3
Tidal volume (L)	1	1	0.2e-3	0.22e-3
Frequency (breaths/min)	15	30	332	572

Steady inhalation conditions were simulated with physiologically realistic flow-rate conditions. Two inhalation conditions, i.e. rest and light exertion, were simulated and compared between the human and mouse models (Table 1). During inhalation an inlet mass flowrate boundary condition was applied at the nostrils and a constant pressure was assumed at the outlets. During exhalation an outlet mass flow rate was applied at the nostrils. Typical human rest and light exertion breathing flow rates are 15 LPM (L/min) and 30 LPM (Kolanjiyil and Kleinstreuer, 2016), whereas 0.066 LPM and 0.125 LPM are the simulated mouse inhalation flowrates (DeLorme and Moss, 2002), as summarized in Table 1. CF-PD simulations were conducted using Ansys Fluent 17 (ANSYS Inc., Canonsburg, PA). The flow field solution was assumed as converged when the mass and momentum residuals dropped by at least three orders of magnitude and did not vary with further iterations.

2.3. CF-PD modeling equations

2.3.1. Airflow

The Shear Stress Transport (SST) k-ω turbulence model was employed to simulate the laminar, transitional and fully turbulent flow regimes in the human nasal-upper airways and a laminar model was used in the mouse nasal-upper airways. The SST k-ω turbulence model has been found to predict accurately and cost-effectively the transitional, turbulent flows and particle transport in nasal and oral airway models and tracheobronchial airway bifurcations (Zhang and Kleinstreuer, 2011). The Reynolds-averaged Navier-Stokes equations (RANS) are commonly used to describe conservation of mass and momentum for laminar-transitional-turbulent flow:

$$\frac{\partial \bar{u}i}{\partial xi} = 0 \tag{1}$$

$$\overline{uj}\frac{\partial \bar{u}i}{\partial xj} = -\frac{1}{\rho}\frac{\partial \widehat{p}}{\partial xi} + \frac{\partial}{\partial xj}[(\nu + \nu t)(\frac{\partial \bar{u}i}{\partial xj} + \frac{\partial \bar{u}j}{\partial xi})] \tag{2}$$

Here $\bar{u}_{\,i}$ is the time-averaged velocity in three coordinate directions, i.e., $i = 1$, 2, and 3, $\widehat{p}$ is the modified time-averaged pressure term, ρ is the fluid density, ν is the kinematic viscosity and νt is the turbulent flow viscosity.

The transport equations governing turbulent kinetic energy (k), specific dissipation rate (ω) and other submodels with additional functions for the SST k-ω turbulence model are given in Zhang and Kleinstreuer (2011). All transport equations were discretized to be 2nd order accurate in space.

2.3.2. Particle transport and deposition modeling

Particle transport of dilute nano- and micro-sphere suspensions (50 nm $<$ d $<$ 15μm) with a high density-ratio of particle-to-air, was modeled using a one-way coupled Lagrangian approach, assuming particle rotation and thermophoretic forces. Specifically,

$$\frac{dx_i^p}{dt} = u_i^p \tag{3}$$

$$m_p \frac{du_i^p}{dt} = F_i^D + (m_p - m_f)g_i \tag{4}$$

where m_p and m_f are the mass of particle and fluid. For our modeling analysis we assumed that the major point forces acting on each particle are the drag and gravity. For submicron particles ($d_p \leq 1\mu m$) the effects of Brownian diffusion were also considered. The drag force is calculated as,

$$F_i^D = \frac{\pi}{8}\rho_f d_p^2 C_D (u_i^f - u_i^p)|u_i^f - u_i^p| \tag{5}$$

where ρ_f is the fluid density, d_p is the particle diameter, u_i^f is the fluid velocity at particle center, u_i^p is the particle velocity, and C_D is the Schiller-Naumann drag coefficient, g_i is the gravitational vector. Clearly, when the particle density is unity (1g\cm^3), the particle diameter d_p is equivalent to its aerodynamic diameter d_a. The unity-particle-density was employed to allow for straightforward comparisons with experimental data sets, which are mostly reported in terms of d_a. Due to the assumption of dilute particle suspensions, the momentum transfer from particles to the fluid phase is neglected. Initial analysis of particle deposition in a human nasopharyngeal model during inhalation at 10 LPM and 20 LPM with 50 nm, 100 nm and 400 nm spheres assuming Stokes drag and the gravitational force and with and without the Cunningham slip correction factor the difference in deposition for all the cases was less than 0.1%. Hence, for the particle sizes considered in this study any impact of the Cunningham slip correction factor was neglected.

Then, the particle deposition efficiency is defined as:

$$DE = \frac{N_{dep}}{N_{in}} \tag{6}$$

where N_{dep} is the number of particles deposited on the surface area of interest, which can be the nasopharyngeal wall or local surface areas, e.g. olfactory regions, and N_{in} is the total number of particles released at the nostrils.

The magnitude of the Brownian force per unit mass is given by:

$$F_i^{Brownian} = \varsigma_i \sqrt{\frac{\pi S_o}{\triangle t}} \tag{7}$$

where ς_i is a zero mean variant from a Gaussian probability density function, S_o is a spectral intensity function directly related to the diffusion coefficient, and $\triangle t$ is the time-step for particle integration. Many recent articles have shown that Fluent Brownian motion model produces erroneous particle trajectories as the Brownian model (affected by the selection of timestep and mesh density). It can be corrected by using a Brownian motion model prescribed by a UDF which has been shown to be unaffected by the timestep selection (Longest and Xi, 2007; Inthavong et al., 2011, 2016). The Brownian force term was incorporated into the particle transport equation using a User Defined Function (UDF) where a time step of 10^{-6} s was selected, employing another UDF.

3. Particle deposition in the lower lung airways

The aerosol deposition per generation in the lower and alveolar mouse and human lung airways were estimated using a deterministic lung deposition model. As high-resolution lung-airway images are not available, typical path lung-airway models made of cylindrical bifurcations for both human and mouse configurations were considered. Specifically, the CF-PD deposition results in the nasopharyngeal region and tracheobronchial airways were coupled with the deterministic lung deposition model for airways from generation 4 onwards (ie, model details are provided in the supplementary materials). The airway parameters of the mouse lung airways (as reported by Oldham and Robinson, 2007) and those of humans are listed in the supplementary materials. The mouse lung morphometric model is a typical path model rescaled to functional residual capacity (FRC) of 0.65 ml which is in accordance with the reported data (Oldham and Robinson, 2007; Sakoda et al., 2012; Asgharian et al., 2014). The human lung morphometric model is a typical path model rescaled to FRC of 3000 ml (Yeh and Schum, 1980; Yu and Diu, 1982). Both mouse and human lung geometries were again rescaled to an average lung volume of $V_{FRC} + V_T/2$, to account for the change in airway dimensions during inspiration and expiration (where V_T is the tidal volume).

The probability of a particle to deposit in an airway segment in terms of the deposition efficiency (DE), depends mainly on three deposition mechanisms, ie, diffusion, impaction, and sedimentation (Zhang et al., 2008). The deterministic approach to estimate airway deposition in a given typical path lung-airway model has been presented previously (Goo and Kim, 2003; Asgharian et al., 2014). Recommended deposition probability equations (given in the supplementary materials), were used to estimate the lung deposition (Yeh and Schum, 1980; NCRP, 1997).

4. Multicompartmental model to predict clearance and migration of deposited nanoparticles

To demonstrate how the present CF-PD results can be combined with pharmacokinetics modeling we applied a physiologically based compartmental kinetics model to predict the retention and translocation of inhaled nanoparticles. Recently, we proposed a mathematical model that can be utilized for pharmacokinetic cross-species extrapolation of lung deposition and retention data from rat to human lungs (Kolanjiyil and Kleinstreuer, 2013). The multi-compartment model consists of the nanomaterial mass transfer routes into the olfactory, bronchial, bronchiolar, and alveolar regions and its migration into the systemic system. The model parameters were determined from experimental retention and clearance data in rodent lungs, and then the validated model was applied to humans based on our pharmacokinetic cross-species extrapolation correlation (Kolanjiyil and Kleinstreuer, 2013). Epithelium/interstitium was considered as separate compartments in each region, except in the olfactory bulb, because ultrafine particles can easily cross epithelial cells and reach the interstitium. During the inhalation process particles are mainly deposited in the olfactory, mucus membrane in bronchi and bronchioles and surfactant layer in alveolar region. For simplification, particles were assumed to finally accumulate in the gastrointestinal tract, lymph, interstitial granuloma, and secondary organs. The retention and clearance of particles from the lung depend on the site at which the particles are deposited and their physicochemical characteristics. Clearance is rapid for particles that deposit in the upper airways compared to that for the particles that deposit in the gas exchange (alveolar) region of the lung. Particles that deposit on the surface of the tracheobronchial region are trapped in the mucus layer that covers the surface of the trachea and bronchi. Particles that are deposited in the terminal bronchioles and the alveolar region will be phagocytized by macrophages which transport them to the upper bronchioles for clearance through the mucociliary escalator. After crossing the epithelial cell barrier, the free nanoparticles in the interstitium can easily reach the lymphatic system or systemic circulation. Alternatively, they are phagocytized by interstitial macrophages and transported back to the airways or to the lymphatic system. Similarly ultrafine particles which are deposited in the olfactory region can be transported from the nasal olfactory mucosa to the olfactory bulb by axonal transport via the olfactory nerve. Assuming an average Balb/c mouse body weight of 0.03 kg, following the methodology for pharmacokinetic time scale scaling (Kolanjiyil and Kleinstreuer, 2013), the transfer rate coefficients for the mouse model were obtained by multiplying the (available) transfer rate coefficients

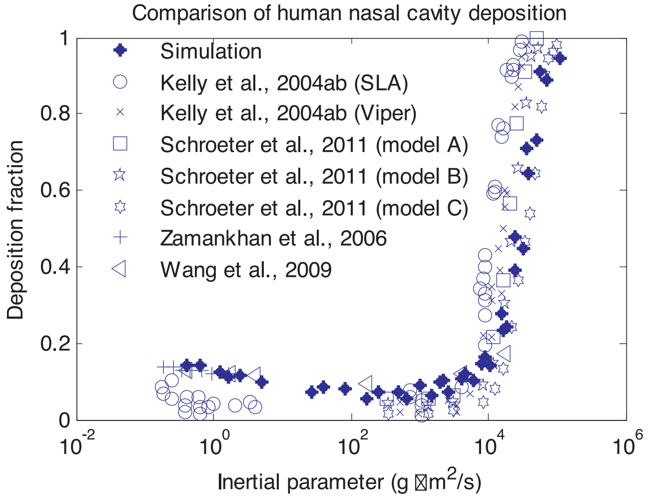

Fig. 2. Comparisons of particle deposition in the human nasal cavity with experimental and other numerical results.

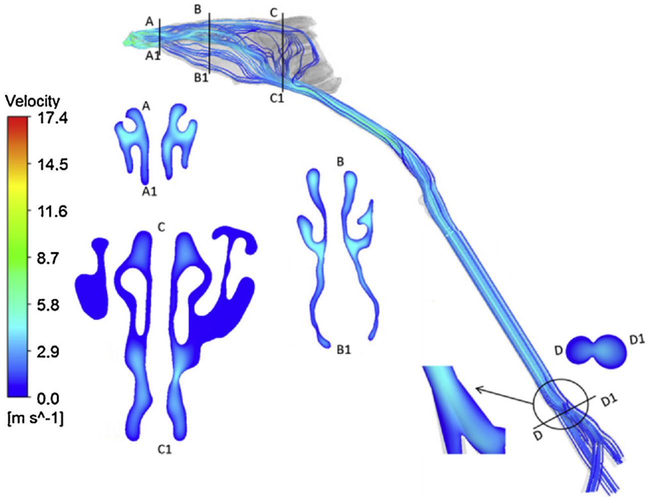

Fig. 3. Airflow in mouse lung airways at breathing under light exertion condition. Airway cross-sections A–D are shown in detail.

of a rat model by a pharmacokinetic time scale factor. The human model transfer coefficients are reported in (Kolanjiyil and Kleinstreuer, 2013).

5. CF-PD model validation

In order to validate the current CF-PD modeling approach (see Fig. 2), the particle deposition results predicted in the human nasal cavity using CF-PD were compared with experimental data (Kelly et al., 2004a,b) and other numerical results from the published literature (Zamankhan et al., 2006; Wang et al., 2009; Schroeter et al., 2011). SLA and Viper refer to nasal replicas manufactured with different rapid prototyping machines (Kelly et al., 2004a,b). In order to provide reproducibility and clarity, the results were plotted in terms of the impaction parameter (IP), *viz:*

$$IP = \rho d^2 Q \tag{8}$$

Here ρ is the particle density in g/cm^3, d is the particle diameter in μm, and Q is the volumetric airflow rate in cm^3/s. The CF-PD deposition study was conducted for inhalation flow rates of 10 LPM, 15 LPM and 20 LPM. The experimental measurements were made for inhalation flow rates of 10 LPM and 20 LPM. Good agreement was observed between the CF-PD deposition results and experimental data points. Shi et al. (2007) and Schroeter et al. (2011) had numerically confirmed the findings of Kelly et al. (2004a,b), that the variability in nasal deposition results is due to the effect of differences in wall roughness in the *in vitro* models, which may contribute to increased capture of larger particles. For submicron particle sizes considered in this study, that mechanism is negligible as these particles closely follow the streamlines even when surface roughness influences the flow field near the wall (Zamankhan et al., 2006; Wang et al., 2009).

6. Results and discussion

The airflow and particle transport/deposition in both the mouse and human respiratory tract models were simulated under steady rest and light exertion conditions using CF-PD (see Table 1). As the airway-branching patterns are primarily dichotomic in human lungs and monopodial in mouse lungs, the airflow patterns and hence local particle depositions were different.

6.1. Airflow in the mouse and human upper-airways

Fig. 3 depicts the flow streamlines through the mouse nasal and upper lung airways at light exertion inhalation/exhalation conditions. The data provide a quantitative visualization of the flow behavior captured by tracking massless particles, ie, essentially streamlines. They were released from the nasal inlets, where the flow patterns traversing the left and right nasal passages are identical (slice A-A1). The reduction in cross-sectional area after the nasal vestibule induces accelerated airflow and creates secondary velocity components (slice B-B1). The trajectories of the flow streamlines were traced back to the release position from the surface plane of the nares in order to correlate the flow path to its origin. The flow streamlines originated from the dorsal side of the naris, travelled to ethmoidal and olfactory regions, and exited to the nasopharyngeal region following an S-shaped path. The streamlines originated from the lateral side of the external naris followed a path closer to the nasal cavity floor and exited directly into the nasopharyngeal region (see increased flowrate at the nasal cavity floor in slice C-C1).

The change in cross-sectional area is minimal at the glottis, and hence the laryngeal jet effect is minimal. The presence of secondary flow characteristics is also small in the glottis and epiglottis regions. The transition of the airflow from the nasopharyngeal region to the tracheobronchial region is smooth, where due to the elongated structure of the trachea the flow becomes parabolic. Because the tracheobronchial airway structure of a mouse lung is mostly monopodial in nature, the main airflow continues its path through the main airway (Fig. 3). While the airflow division from the parent airway to the daughter airways is highly asymmetric (slice D-D1), the secondary vortices developed in the bifurcation regions are small because of the lower branching angles. In order to compare the airflow results between different breathing conditions, and with human inhalation results, the average Reynolds numbers were measured at the end of the trachea. For example, the average Reynolds number measured at the end of trachea during light exertion breathing condition was 165.

The velocity fields through the human nasal and upper lung airways for light exertion breathing condition are shown in Fig. 4. The majority of the flow was found to continue through the lower nasal air passages (middle and inferior meatus), thereby protecting the upper olfactory region (slice B-B1). Similar to the mouse case, the reduction in cross sectional area after the nasal vestibule forces the flow to accelerate and create secondary velocity components, which distribute the air to the middle and inferior meatus (slice A-A1). Secondary flow phenomena, such as flow separation and recirculation, can be identified after the flow has passed through the nasal vestibule with an apparent 90° change in flow direction (slice A-A1). In the nasopharynx region, the flow undergoes another 90° change in direction, which again produced

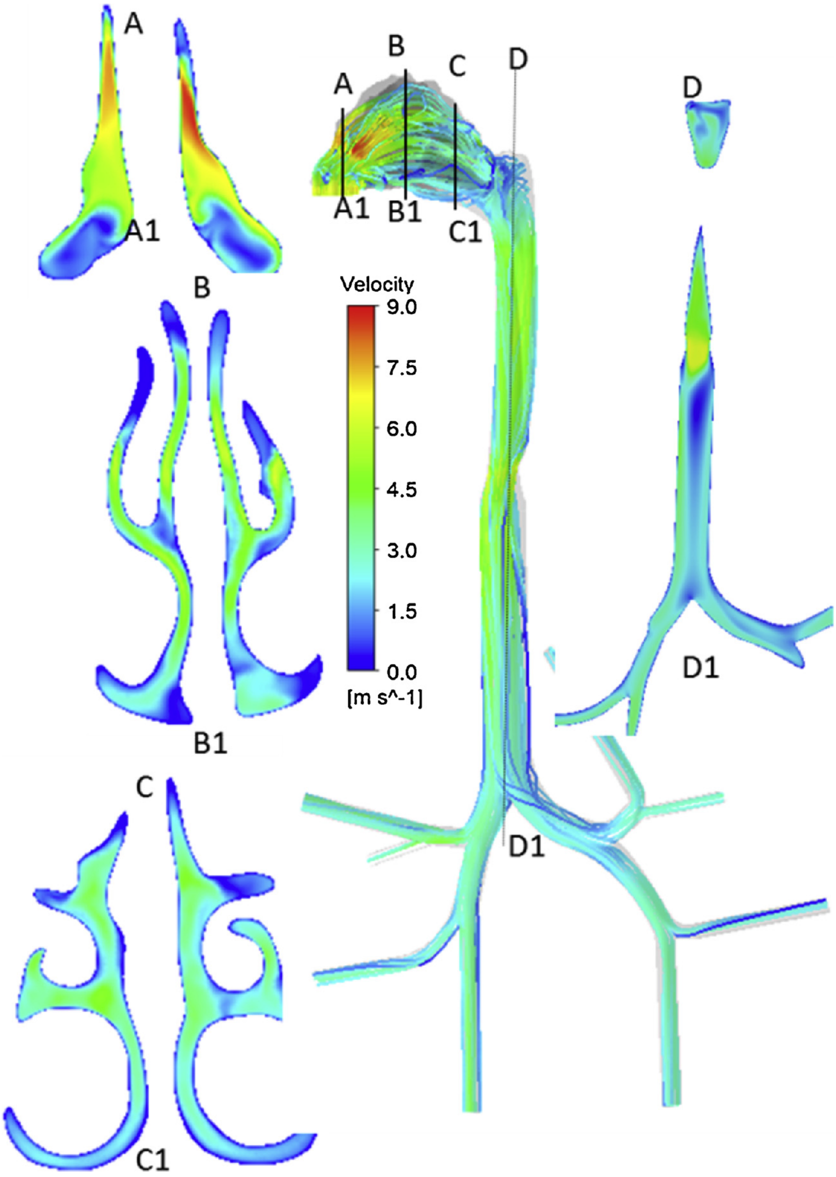

Fig. 4. Airflow in human lung airways at light exertion breathing condition. Airway cross-sections A–D are shown in detail.

secondary flow structures (slice D-D1). Recirculation regions in the nasopharynx are depicted via the airflow streamlines.

Due to the sudden geometric constriction at the glottis, an asymmetric high-speed laryngeal jet was generated, which produced a recirculation zone near the anterior wall of the upper trachea. Because of the secondary flow structures, the velocity profile in the trachea is skewed towards the anterior part. Once the flow advances in the trachea, the velocity profile is redistributed by secondary motion, producing a parabolic velocity profile. Flow separation and recirculation are prominent in the human bronchial airway bifurcation regions (slice D-D1). The flow profile and secondary flow structures in the daughter branches of the bronchial airways were found to vary with the bifurcation angle and daughter tube diameters. As the tracheobronchial airway architecture of a human lung is dichotomic in nature, the airflow division from the parent airway to the daughter airways is mostly symmetrical (see Fig. 4). However, due to the large airway branching angles, the secondary vortices in these regions are prominent. The average Reynolds number measured at the end of trachea during light exertion breathing condition was 2980. In general, compared to the simulation data for the mouse airways, the higher Reynolds number in the human tracheal airway indicates more rapid particle mixing.

6.2. Particle transport and deposition in the mouse and human upper airways

Considering spherical particles in the diameter-range of 50 nm to 15 μm for the human model and 50 nm to 5 μm for the mouse model, their transport and deposition in the nasal tracheobronchial airways were analyzed assuming a one-way coupled Eulerian-Lagrangian formulation. The major point-forces for the submicron particle sizes considered in this study were drag, gravitational (fully in vertical direction) and Brownian forces (for diameters $< 1\mu m$). The particle-deposition results in both mouse and human nasopharyngeal regions are shown in Figs. 5 and 6, respectively. In the mouse model, there is an exponential increase in nasopharyngeal deposition for particle sizes greater than 2 μm due to inertial effects; in contrast, for the human model the threshold diameter is around 6. With the increase in inhalation flow rate, this threshold diameter decreases. For particle sizes less than 2, the deposition fraction in the mouse nasopharyngeal region is similar to that of the human model. For sub-micron particles, the deposition in the mouse nasopharyngeal region at rest is slightly higher than at light exertion while in the human nasopharyngeal region, the deposition at rest is lower than at light exertion.

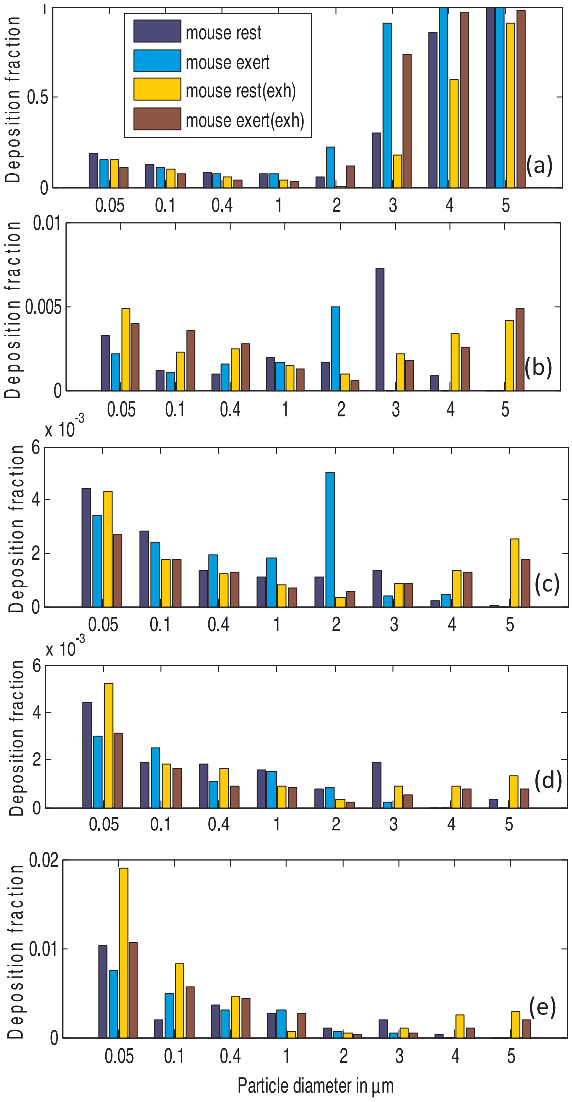

Fig. 5. Particle deposition in mouse nasopharyngeal model: (a) nasopharyngeal; (b) tracheal; (c) generation 1; (d) generation 2; and (e) generation 3.

For the tracheobronchial regions of the mouse and human models, considerable differences in particle deposition patterns were noted, mainly because of the differences in tracheobronchial airway architecture between mouse and human airways. For instance, particles less than 2 μm deposited mostly in airway generation 3 of the mouse model, followed by generation 1, generation 2, and the trachea. Meanwhile, in the human model particles less than 4 μm deposited predominantly in airway generation 3, followed by generation 2, generation 1 and the trachea. Particle depositions in human airway generations 2 and 3 were higher than those found in the mouse counterparts. However, particle deposition in human airway trachea and generation 1 were lower than that in the mouse airways. In the mouse model, the highest deposition was in the nasal cavity during both inhalation and exhalation phase. In the human model the highest deposition was in the nasal cavity during the inhalation phase, while the highest deposition shifted from the nasal cavity to lower lung airway generations during exhalation phase when the inhaled particle size changed from submicron to micron particles.

When plotting the predictive particle-deposition results for the mouse and human nasopharyngeal models subject to the two breathing modes in terms of the Stokes number, all four curves nearly merged into a single one (see Fig. 7). Here, the Stokes number is defined as $St = \rho_p d_p^2 U/18\mu D = 2\rho_p d_p^2 Q/9\pi\mu D_h^3$ where ρ_p is the particle density (1000 kg/m^3), d_p is the particle diameter, μ is the fluid viscosity, U and Q are the mean tracheal inlet velocity (m/s) and flowrate (m^3/s) measured at the tracheal inlet cross-section, and D^h is the smallest hydraulic diameter in the laryngeal region. Recently, Cheng et al., (1999) have shown that the variability in the oropharyngeal deposition can be accounted for by using correlations in terms of smallest hydraulic diameter. Following a similar approach here, we have shown that a similar correlation can even be used for capturing the inter-species variability in the nasopharyngeal deposition. The smallest hydraulic diameters are 1.08 cm and 0.096 cm for the human and mouse models, which is 67% and 87% of the tracheal diameters. It is an apparent particle-deposition paradox that there are significant morphological differences between the mouse lung model to that of the human airways, yet the *overall* particle deposition is nearly the same. Clearly, use of the smallest hydraulic diameters as the characteristic dimension turned out to be beneficial for estimating the Stokes number during cross-species extrapolation of the inhaled dosage. This similarity could be explored further for pharmacological crosspieces extrapolation of rodent data to humans. Specifically, the mouse nasal deposition could be reproduced in a human by designing aerosol inhalation systems with identical Stokes number for both mouse and human. This will ensure similar aerosol deposition fraction (DF) in the nasopharyngeal region of both mouse and human; the new DF(St)-correlation is given in Eq. (9). The relation was derived by curve-fitting the mouse and human nasopharyngeal deposition data with an R-square value of 0.978 for the inhalation deposition data and 0.84 for the exhalation data after excluding the human nasopharyngeal deposition for particles above 10 μm.

$$DF = 1 - 0.88\exp(-1049\ St^{2.5}) \tag{9}$$

The particle deposition patterns in the mouse and human nasal-tracheobronchial models at light exertion breathing are plotted in Figs. 8 and 9. The deposition in the lung airways is not uniform in the lower airways; for example, in generation 3 significant differences were noticed among different branches. Clearly, a CF-PD study is warranted to accurately predict high-resolution deposition patterns in complex lung geometries. The results indicate that the nanoparticles (having low inertia) tend to adapt to the changes in the flow path and hence show higher dispersion. The particle dispersion increased with decrease in particle diameter, which eventually resulted in more uniform deposition of submicron particles on the airway walls. With the increase in particle inertia, the gravitational sedimentation force becomes dominant and the particles tend to deviate from the flow paths, ie, streamline crossing occurs, resulting in concentrated deposition patterns (hot spots). Irrespective of the species, the particle deposition has a maximum in the entrance region of the nasal passages. This is due to the local geometrical constriction of the nasal passage leading to higher air velocities and hence larger impaction. However, for a given breathing condition, the particle deposition in the mouse nasal cavity is slightly higher than in the human counterpart. It was also observed that the particles have a higher tendency to deposit on the carinal ridges of the bifurcations, particularly as the particle size increases. It appears that human airway bifurcations exhibit higher depositions than seen in the mouse, likely due to the larger bifurcation angles in the lower human airways.

6.3. Total deposition in mouse and human lungs

We estimated the total lung deposition by coupling the CF-PD deposition results in the nasopharyngeal region and tracheobronchial airways with the deterministic lung deposition model for airways from generation 4 onwards. First we compared the total lung particle deposition predicted by our hybrid mouse model with experimental measurements. To our knowledge, there is limited experimental data available in the literature on mouse-lung deposition. This is compounded by the fact that most reports lack information on the mouse

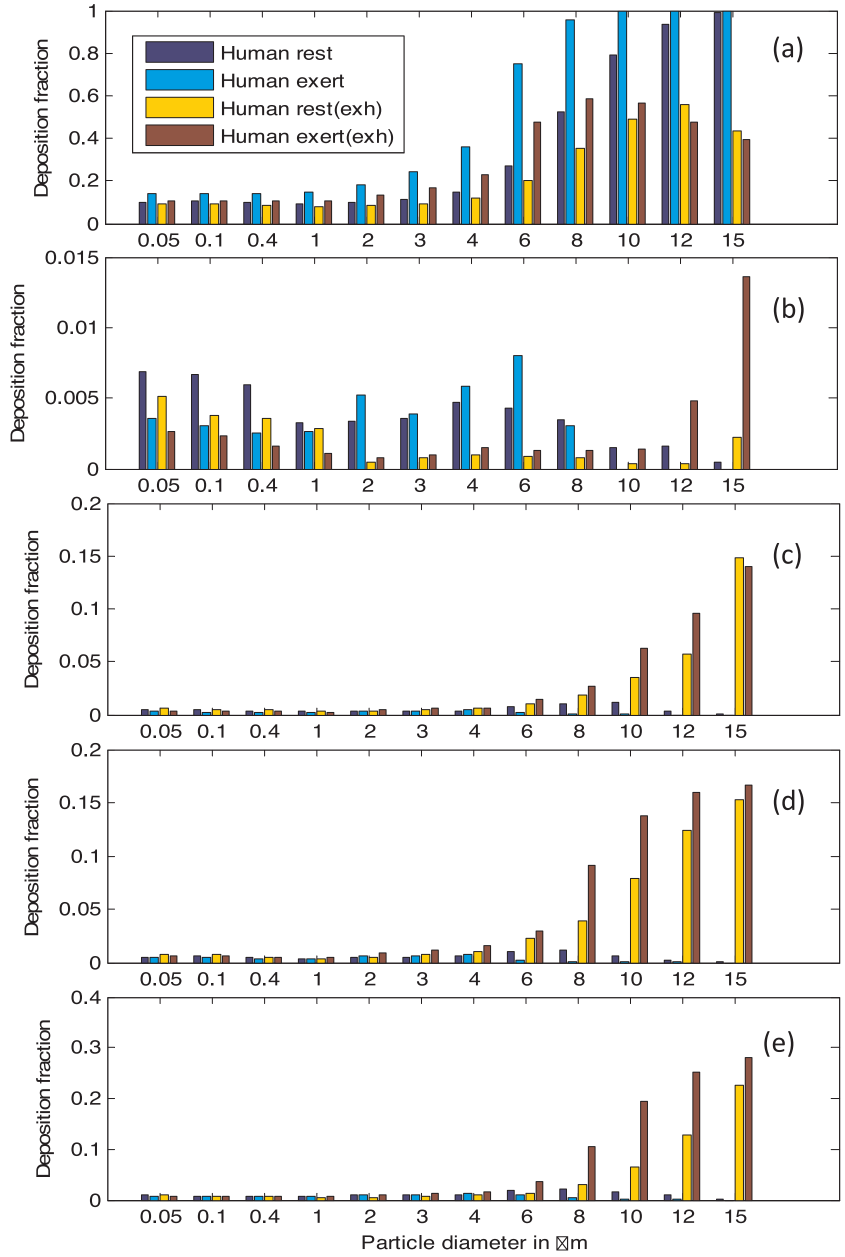

Fig. 6. Particle deposition in human nasopharyngeal model: (a) nasopharyngeal; (b) tracheal; (c) generation 1; (d) generation 2; and (e) generation 3.

ventilatory parameters as well as particle clearance from gastrointestinal area and other secondary locations. In addition, differences in the mouse strain and experimental setup contribute to deposition variability. We considered an inhalability fraction because only a portion of the particles from the ambient air is inhaled (Menache et al., 1995). The experimental studies from the literature were conducted using Balb/c mouse (Alessandrini et al., 2008; Oldham et al., 2009), B6C3F$_1$ mouse (Hsieh et al., 1999; Kuehl et al., 2012), C57BL/6 mouse (Nadithe et al., 2003), and CF$_1$ mouse (Raabe et al., 1988) strains. After taking into consideration the upper lung airway deposition from CF-PD models, deposition results for the mouse lung at light exertion demonstrated reasonable agreement with experimental measurements especially with Balb/c mouse strain (see Fig. 10). Clearly, the predicted lung depositions for both sub-micron and larger particles followed the trends of the experimental studies; however, some differences can be attributed to the uncertainties related to mouse type and polydisperse particles.

Next we simulated the deposition in human lung using the hybrid model, taking into account the deposition results from the CF-PD simulations. Assuming that the drug-aerosols are administered directly into the nose, we neglected the inhalability fraction for the human lung simulation. As shown in Fig. 11, the model predicts particle lung deposition for breathing at rest similar to the data obtained from experimental measurements (Heyder et al., 1986). Since deterministic human lung deposition results have been discussed in detail previously, we have only simulated here a typical flow rate of 15 LPM with tidal volumes 500 ml and 1000 ml for particle diameters in the range 50 nm to 10 μm. Small variations in the deposition results are due to the differences in the nasopharyngeal filtration of the upper micron particles by the subject specific extrathoracic geometry.

After validating the hybrid models, we compared the total deposition (thoracic and extrathoracic) and lung deposition (thoracic) at different breathing conditions for both mouse and human cases (see Fig. 12a and 1b). The shape of the deposition curve for each flow rate is essentially maintained for both species at submicron particle sizes and demonstrates clear non-monotonicity. The total deposition is higher for

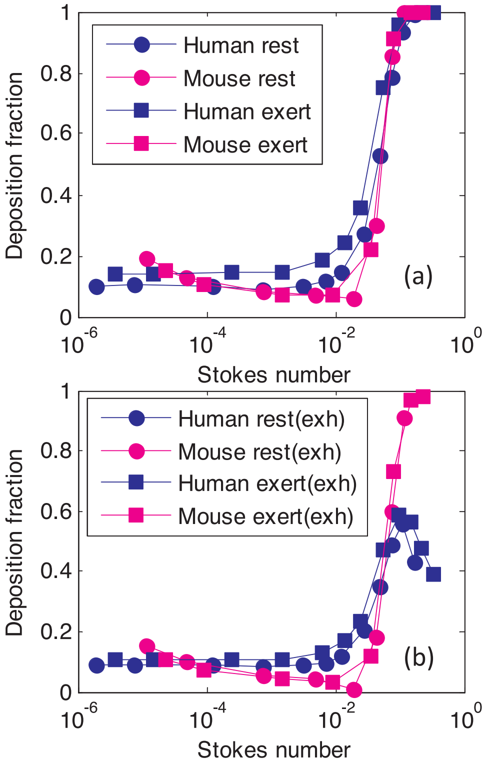

Fig. 7. Comparison of particle deposition results between mouse and human nasopharyngeal models (a) inhalation (b) exhalation.

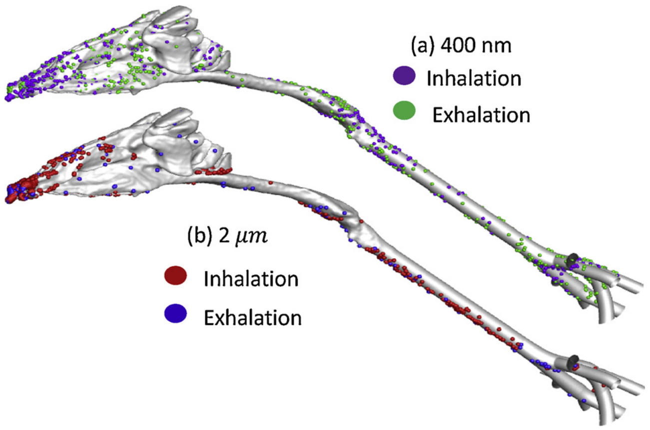

Fig. 8. Particle deposition pattern in mouse nasal-tracheobronchial model with breathing at light exertion for particle size: (a) 400 nm; and (b) 2μm.

submicron particles of low diameters, whereas for micron particles, the deposition increases with larger particle diameters. Minimal deposition is observed for particle size around 1 μm in both species for all breathing conditions considered. Due to the pre-filtration effect of the inhalability fraction, the total deposition in the mouse lung declines for diameters above 2. Hence it is not advisable to use mice as a human surrogate for pharmacological and toxicological studies with particle sizes above 2. Even though the inter-species differences in total deposition are slight, lung deposition is within close range only for the submicron particles (see Fig. 12b). For submicron particles, the mouse lung deposition is slightly higher than human lung. For micron particles, the deposition in human lung airways is much higher than that in mouse lung airways. This higher deposition of micron particles in human lung airways can be attributed to the reduced filtration in the nasopharyngeal region compared to mouse nasopharyngeal filtration. In addition, deposition in the mouse lung is further reduced by the inhalability fraction. Following the total deposition trend, lung deposition also has a minimum around 1. Particle deposition in the lung increases with particle size in the micron range, reaching a peak and then declining to zero. In the micron range, the lung deposition is at a maximum around 2 μm for the mouse and around 4 μm for the human under rest condition. The lung deposition peak shifts to the left when the flowrate increases. These insights have implications for future dug delivery experiments, where the lower lung airways are the preferred destination for drugs/vaccines, and for toxicology studies where systemic exposure is of concern.

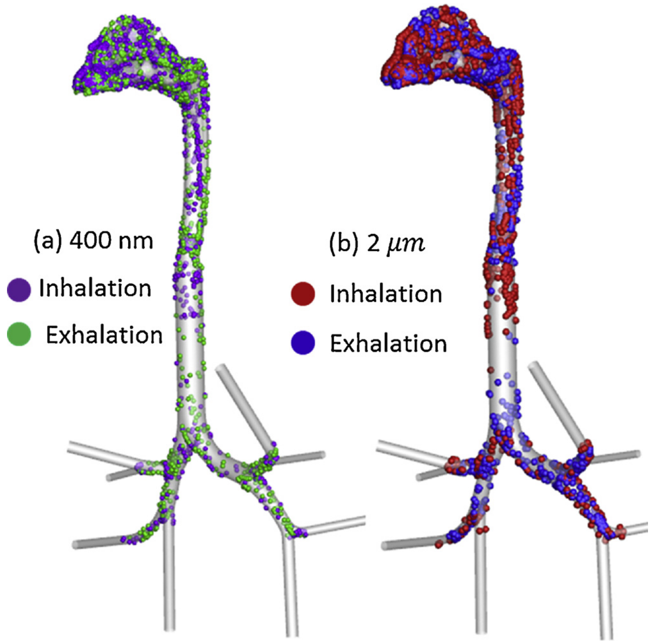

Fig. 9. Particle deposition pattern in human nasal-tracheobronchial model with breathing at light exertion for particle size: (a) 400 nm; and (b) 2μm.

We also compared the deposition in the tracheobronchial and alveolar regions of mouse and human models as shown in Fig. 13a and b. Similar to the lung deposition, the tracheobronchial and alveolar deposition fractions in the human model are comparable to that in the mouse model for submicron particles. For micron particles, the tracheobronchial deposition and alveolar deposition are significantly higher in the human lung than that in the mouse.

While comparing the deposition in individual lung airway generations, we noted significant differences in deposition trends. As shown in Fig. 14a, for 400 nm particles the deposition in the mouse and human upper airway generations are similar. However, the deposition starts to vary with an increase in generation number, reaching significant deposition variations in the lower lung regions. Specifically, the submicron deposition in the human distal lung airways is consistently lower than that in mouse-airway generations. For micron particles, as shown in Fig. 14b, deposition in the human distal lung airways are higher than that in mouse-lung airways. However, the differences in deposition between mouse and human lung airways are significant only at the terminal airway generations.

6.4. *Clearance and migration of deposited nanoparticles*

After estimating the drug aerosol deposition in mouse and human lung models, the dosage (mg) for animal or human exposure can be expressed as follows:

$$Dosage = Aerosol\ Concentration\ *\ Breathing\ frequency\ *\ Tidal\ volume\ *\ Time\ *60*Deposition\ fraction \qquad (10)$$

where Concentration is in mg/m^3, Breathing frequency is the number of

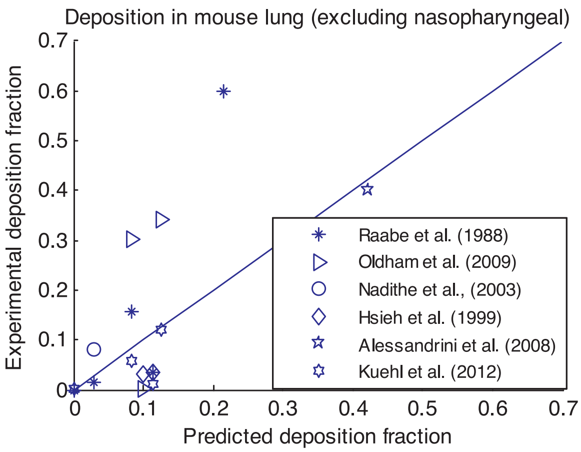

Fig. 10. Comparison of predicted mouse lung deposition with the experimental measurements.

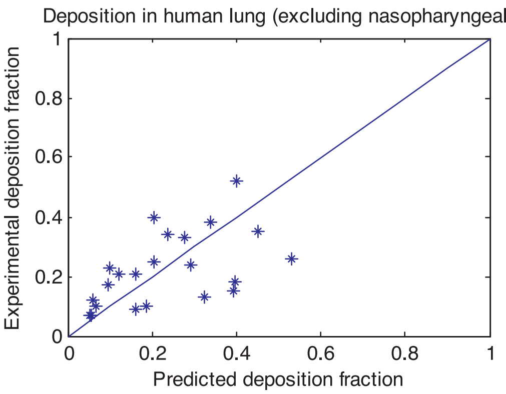

Fig. 11. Comparison of predicted human lung deposition with the experimental measurements.

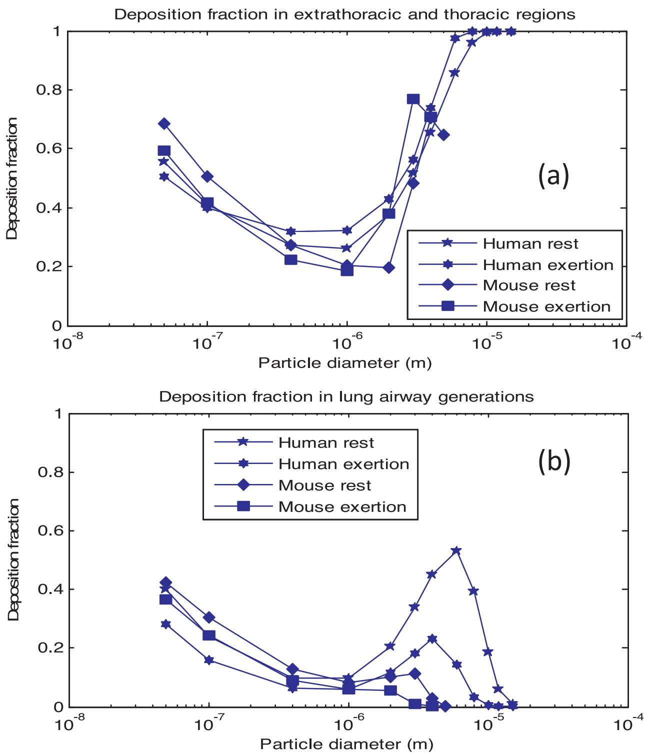

Fig. 12. Comparison of predicted deposition between mouse and human (a) total; and (b) lung.

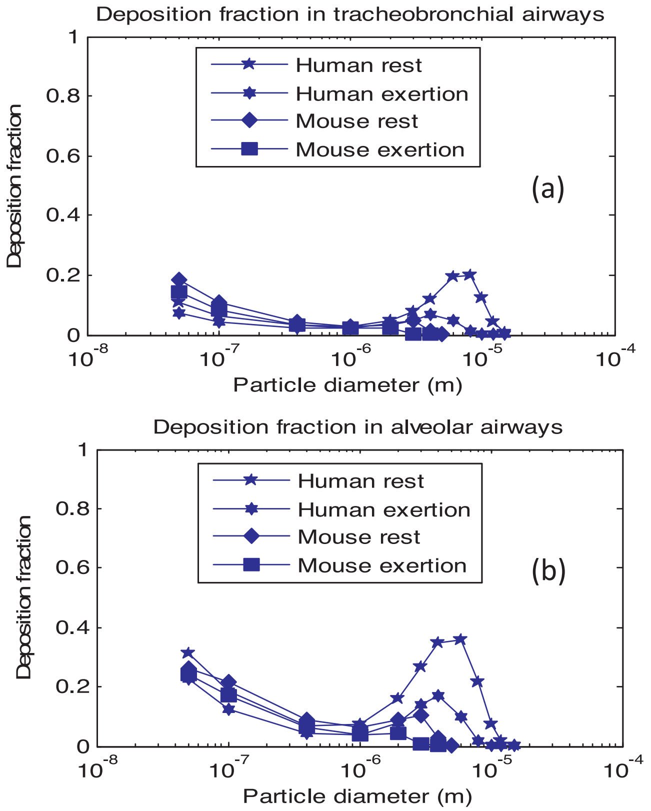

Fig. 13. Comparison of predicted deposition between mouse and human (a) tracheobronchial airways; and (b) alveolar airways.

breaths per minute, Tidal volume is in m^3, Time is the exposure time in hours, and the deposition fraction is numerically predicted. Specifically, the output from the CF-PD simulations determined the deposition concentrations of the nanoparticles in key segments of the human respiratory system, which in turn were used as the initial condition for the multi-compartment model (ie, PBPK model). The amount of inhaled mass retained in the lung after exposure and the amount transferred to the circulatory system, lymphatic system and other organs were predicted in both species (see Fig. 15). For the mouse, a nose-only exposure of 50 nm particles with a concentration of $20\,mg/m^3$ for 4 h. was assumed, while for the human case, direct inhalation of 50 nm particles with a concentration of $20\,mg/m^3$ for 15 min was assumed. Fig. 15 shows the comparison of particle retention and translocation kinetics in the mouse and human lungs. The initial deposition assuming the current exposure condition was 234 μg in the mouse lung airways and 90 μg in the mouse nasopharyngeal airways. In contrast, it was 10 μg in human lung airways and 5 μg in human nasopharyngeal airways. As shown in Fig. 15a and b, the particle retention kinetics predict that clearance from the human lung is slower than in the mouse lung. Fig. 15c and d indicate the amount of nanoparticles translocated to the lymphatic system and the blood circulation system from the lung airways, including the alveolar region. The amount of nanomaterial reaching these regions is higher in the mouse considering the higher initial lung deposition. Fig. 15e depicts the amount of nanoparticles translocated to other organs from the blood circulation system. Organs such as the liver, kidney, spleen, brain and heart, where nanoparticles may deposit through blood circulation, were modeled as a closed compartment, labeled "other organs," without any clearance from them. Around 5% of the initial deposited nanomaterial reaches other organs from the mouse lung, while around 4% of the initial deposited nanomaterial reaches other organs from the human lung. Fig. 15f displays the amount of nanoparticles translocated to the olfactory bulb in

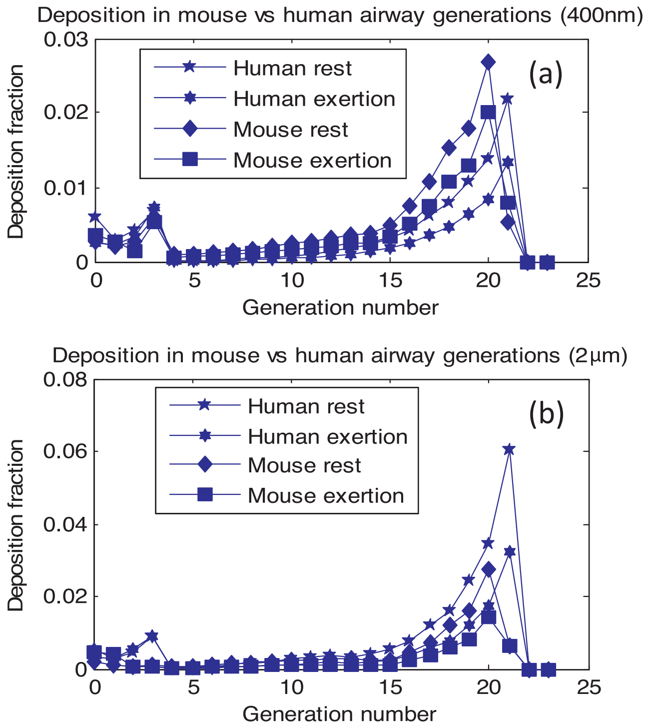

Fig. 14. Comparison of predicted deposition between mouse and human lung airway generations (a) 400 nm; and (b) 2 μm.

the brain. Considering that the mouse olfactory region is larger and the initial deposition in the nasopharyngeal region is one order of magnitude higher than that in humans, around 3 μg of nanomaterial reaches the mouse brain while the human brain receives only 0.03 μg, two orders of magnitude less. Clearly, this indicates that for nose to brain delivery of drugs, the extrapolation of results from rodents to humans must be conducted with great caution.

7. Conclusions

In this study, the particle depositions in various regions of representative human and mouse lung models were compared, using a hybrid modeling approach. The deposition in the nasopharyngeal region significantly influences the deposition in the lower lung regions. In the mouse model, the nasopharyngeal deposition exponentially increases with particle diameter for particle diameters above 2 μm, while it filters out most of the particles above 3 μm. Hence, it is not advisable to use mice as a human surrogate for pharmacological or toxicological studies with particle sizes above 3 μm. For particle sizes less than 2 μm, the deposition fraction in the mouse nasopharyngeal region is comparable to that for the human model. Similarly, the total deposition data indicate that the total particle deposition fractions are in close range in the respiratory models of mice and humans under corresponding breathing conditions. However, considerable differences were noted in *local* particle deposition pattern between the lung airway generations of mouse and human models. This is because of the differences in the tracheobronchial airway architecture of the mouse and human airways. Nevertheless, the particle deposition results in both mouse and human nasopharyngeal models collapsed into a single curve

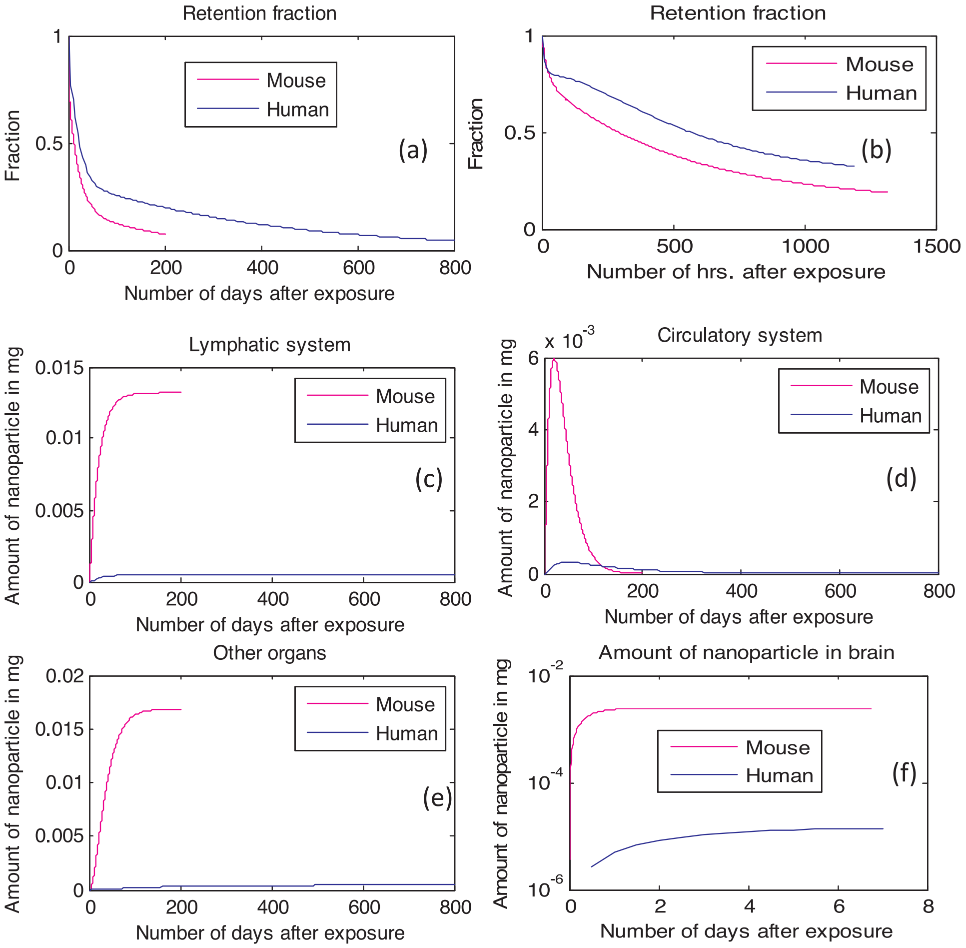

Fig. 15. Comparison of particle retention and translocation kinetics in the mouse and human lungs.

when plotted against the Stokes number with the smallest hydraulic diameter being the characteristic dimension. As a result, a new, easy-to-use correlation between the particle deposition fraction and the designated Stokes number was obtained. Combined with the deposition model, the particle retention and clearance kinetics of deposited nanoparticles indicates that the clearance rate from the mouse lung is higher than that in the human lung. Hence, the translocation of nanomaterial from the deposited lung sites to other systemic regions occurs at different rates in mice and humans. Similarly, the amount of nanomaterial reaching the human brain is two orders of magnitude less than that in the mouse brain.

In summary, the new hybrid modeling methodology can be employed, and further advanced, for cross-species extrapolation of administered dosages of toxic or therapeutic aerosols. Specifically, the predicted mouse-and-man local and total depositions of inhaled/exhaled aerosols are of interest to drug developers, toxicologists, and regulators alike.

Declaration of interest

None.

Acknowledgements

The authors gratefully acknowledge Dr. Rick Corley and colleagues at Pacific Northwest National Laboratory for providing the representative mouse nasopharyngeal geometry. The authors acknowledge the use of Fluent and ICEM software from Ansys, Inc. (Canonsburg, PA) as part of the NCSU-Ansys Professional Partnership. This work was partially funded by a grant from NIH, R01CA16700.

Appendix A. Supplementary data

Supplementary material related to this article can be found, in the online version, at doi:https://doi.org/10.1016/j.resp.2018.11.003.

References

Alessandrini, F., Semmler-Behnke, M., Jakob, T., Schulz, H., Behrendt, H., Kreyling, W., 2008. Total and regional deposition of ultrafine particles in a mouse model of allergic inflammation of the lung. Inhal. Toxicol. 20 (6), 585–593.

Asgharian, B., Price, O.T., Oldham, M., Chen, L., Saunders, E.L., Gordon, T., Mikheev, V.B., Minard, K.R., Teeguarden, J.G., 2014. Computational modeling of nanoscale and microscale particle deposition, retention and dosimetry in the mouse respiratory tract. Inhal. Toxicol. 26 (14), 829–842.

Calmet, H., Kleinstreuer, C., Houzeaux, G., Kolanjiyil, A.V., Lehmkuhl, O., Olivares, E., Vazquez, M., 2018. Subject-variability effects on micron particle deposition in human nasal cavities. J. Aerosol Sci. 115, 12–28.

Cheng, Y.S., Zhou, Y., Chen, B.T., 1999. Particle deposition in a cast of human oral airways. Aerosol Sci. Technol. 31 (4), 286–300.

Corley, R.A., Kabilan, S., Kuprat, A.P., Carson, J.P., Minard, K.R., Jacob, R.E., Timchalk, C., Glenny, R., Pipavath, S., Cox, T., 2012. Comparative computational modeling of airflows and vapor dosimetry in the respiratory tracts of rat, monkey, and human. Toxicol. Sci. 128 (2), 500–516.

DeLorme, M.P., Moss, O.R., 2002. Pulmonary function assessment by whole-body plethysmography in restrained versus unrestrained mice. J. Pharmacol. Toxicol. Methods 47 (1), 1–10.

Geiser, M., Kreyling, W.G., 2010. Deposition and biokinetics of inhaled nanoparticles. Part Fibre Toxicol. 7 (2), 1–17.

Goo, J., Kim, C.S., 2003. Theoretical analysis of particle deposition in human lungs considering stochastic variations of airway morphology. J. Aerosol Sci. 34 (5), 585–602.

Heyder, J., Gebhart, J., Rudolf, G., Schiller, C.F., Stahlhofen, W., 1986. Deposition of particles in the human respiratory tract in the size range 0.005–15 μm. J. Aerosol Sci. 17 (5), 811–825.

Hsieh, T.H., Yu, C.P., Oberdorster, G., 1999. Deposition and clearance models of Ni compounds in the mouse lung and comparisons with the rat models. Aerosol. Sci. Technol. 31 (5), 358–372.

Inthavong, K., Zhang, K., Tu, J., 2011. Numerical modelling of nanoparticle deposition in the nasal cavity and the tracheobronchial airway. Comput. Methods Biomech. Biomed. Eng. 14 (7), 633–643.

Inthavong, K., Tian, L., Tu, J., 2016. Lagrangian particle modelling of spherical nanoparticle dispersion and deposition in confined flows. J. Aerosol Sci. 96, 56–68.

Jarabek, A.M., Asgharian, B., Miller, F.J., 2005. Dosimetric adjustments for interspecies extrapolation of inhaled poorly soluble particles (PSP). Inhal. Toxicol. 17 (7-8), 317–334.

Kelly, J.T., Asgharian, B., Kimbell, J.S., Wong, B.A., 2004a. Particle deposition in human nasal airway replicas manufactured by different methods. Part II: ultrafine particles. Aerosol Sci. Technol. 38 (11), 1072–1079.

Kelly, J.T., Asgharian, B., Kimbell, J.S., Wong, B.A., 2004b. Particle deposition in human nasal airway replicas manufactured by different methods. Part I: inertial regime particles. Aerosol Sci. Technol. 38 (11), 1063–1071.

Kleinstreuer, C., Zhang, Z., 2010. Airflow and particle transport in the human respiratory system. Annu. Rev. Fluid Mech. 42, 301–334.

Kleinstreuer, C., Feng, Y., Childress, E., 2014. Drug-targeting methodologies with applications: a review. World J. Clin. Cases: WJCC 2 (12), 742–756.

Kolanjiyil, A.V., Kleinstreuer, C., 2017. Computational analysis of aerosol-dynamics in a human whole-lung airway model. J. Aerosol Sci. 114, 301–316.

Kolanjiyil, A.V., Kleinstreuer, C., 2016. Computationally efficient analysis of particle transport and deposition in a human whole-lung-airway model. Part I: theory and model validation. Comput. Biol. Med. 79, 193–204.

Kolanjiyil, A.V., Kleinstreuer, C., 2013. Nanoparticle mass transfer from lung airways to systemic regions–part II: multi-compartmental modeling. J. Biomech. Eng. 135 (12), 121004.

Kolanjiyil, A.V., Kleinstreuer, C., Sadikot, R.T., 2016. Computationally efficient analysis of particle transport and deposition in a human whole-lung-airway model. Part II: dry powder inhaler application. Comput. Biol. Med. 84, 247.

Kuehl, P.J., Anderson, T.L., Candelaria, G., Gershman, B., Harlin, K., Hesterman, J.Y., Holmes, T., Hoppin, J., Lackas, C., Norenberg, J.P., 2012. Regional particle size dependent deposition of inhaled aerosols in rats and mice. Inhal. Toxicol. 24 (1), 27–35.

Li, Z., Kleinstreuer, C., Zhang, Z., 2007. Particle deposition in the human tracheobronchial airways due to transient inspiratory flow patterns. J. Aerosol Sci. 38 (6), 625–644.

Lin, C., Tawhai, M.H., Mclennan, G., Hoffman, E.A., 2009. Computational fluid dynamics. IEEE Eng. Med. Biol. Mag. 28 (3), 25–33.

Longest, P.W., Xi, J., 2007. Effectiveness of direct Lagrangian tracking models for simulating nanoparticle deposition in the upper airways. Aerosol Sci. Technol. 41 (4), 380–397.

Madl, P., Hofmann, W., Oldham, M.J., Asgharian, B., 2010. Stochastic morphometric model of the BALB/c mouse lung. Anat. Rec. 293 (10), 1766–1775.

Menache, M.G., Miller, F.J., Raabe, O.G., 1995. Particle inhalability curves for humans and small laboratory animals. Ann. Occup. Hyg. 39 (3), 317–328.

Minard, K.R., Einstein, D.R., Jacob, R.E., Kabilan, S., Kuprat, A.P., Timchalk, C.A., Trease, L.L., Corley, R.A., 2006. Application of magnetic resonance (MR) imaging for the development and validation of computational fluid dynamic (CFD) models of the rat respiratory system. Inhal. Toxicol. 18 (10), 787–794.

Moss, O.R., Oldham, M.J., 2011. Predicting Balb/c and B6C3F1 mouse sensitivity to inhaled methacholine: impact of calculating lung-airway dimension and airflow distribution. Aerosol Sci. Technol. 45 (7), 821–826.

Nadithe, V., Rahamatalla, M., Finlay, W.H., Mercer, J.R., Samuel, J., 2003. Evaluation of nose-only aerosol inhalation chamber and comparison of experimental results with mathematical simulation of aerosol deposition in mouse lungs. J. Pharm. Sci. 92 (5), 1066–1076.

Namati, J.T., 2009. Phenotype Characterization of Lung Structure in Inbred Mouse Strains Using Multi Modal Imaging Techniques. University of Iowa.

NCRP, 1997. Deposition, Retention and Dosimetry of Inhaled Radioactive Substances. National Council on Radiation Protection and Measurements (NCRP), Bethesda.

Oakes, J.M., Marsden, A.L., Grandmont, C., Darquenne, C., Vignon-Clementel, I.E., 2015. Distribution of aerosolized particles in healthy and emphysematous rat lungs: comparison between experimental and numerical studies. J. Biomech. 48 (6), 1147–1157.

Oldham, M.J., Phalen, R.F., Budiman, T., 2009. Comparison of predicted and experimentally measured aerosol deposition efficiency in BALB/C mice in a new nose-only exposure system. Aerosol Sci. Technol. 43 (10), 970–977.

Oldham, M.J., Robinson, R.J., 2007. Predicted tracheobronchial and pulmonary deposition in a murine asthma model. Anat. Rec. 290 (10), 1309–1314.

Phalen, R.F., Mendez, L.B., 2009. Dosimetry considerations for animal aerosol inhalation studies. Biomarkers 14 (sup1), 63–66.

Phalen, R.F., Mendez, L.B., Oldham, M.J., 2010. New developments in aerosol dosimetry. Inhal. Toxicol. 22 (sup2), 6–14.

Raabe, O.G., Al-Bayati, M.A., Teague, S.V., Rasolt, A., 1988. Regional deposition of inhaled monodisperse coarse and fine aerosol particles in small laboratory animals. Ann. Occup. Hyg. 32 (inhaled_particles_VI), 53–63.

Sadikot, R.T., 2014. The potential role of nano-and micro-technology in the management of critical illnesses. Adv. Drug Deliv. Rev. 77, 27–31.

Sadikot, R.T., 2012. Peptide nanomedicines for treatment of acute lung injury. Meth. Enzymol. 508, 315–324.

Sadikot, R.T., Rubinstein, I., 2009. Long-acting, multi-targeted nanomedicine: addressing unmet medical need in acute lung injury. J. Biomed. Nanotechnol. 5 (6), 614–619.

Sakoda, A., Ishimori, Y., Fukao, K., Yamaoka, K., Kataoka, T., Mitsunobu, F., 2012. Lung dosimetry of inhaled radon progeny in mice. Radiat. Environ. Biophys. 51 (4), 425–442.

Schroeter, J.D., Garcia, G.J., Kimbell, J.S., 2011. Effects of surface smoothness on inertial particle deposition in human nasal models. J. Aerosol Sci. 42 (1), 52–63.

Shang, Y., Dong, J., Inthavong, K., Tu, J., 2015. Comparative numerical modeling of inhaled micron-sized particle deposition in human and rat nasal cavities. Inhal. Toxicol. 27 (13), 694–705.

Shi, H., Kleinstreuer, C., Zhang, Z., 2007. Modeling of inertial particle transport and deposition in human nasal cavities with wall roughness. J. Aerosol Sci. 38 (4), 398–419.

Thiesse, J., Namati, E., Sieren, J.C., Smith, A.R., Reinhardt, J.M., Hoffman, E.A., McLennan, G., 2010. Lung structure phenotype variation in inbred mouse strains revealed through in vivo micro-CT imaging. J. Appl. Physiol. (1985) 109 (6), 1960–1968.

Vasilescu, D.M., Gao, Z., Saha, P.K., Yin, L., Wang, G., Haefeli-Bleuer, B., Ochs, M., Weibel, E.R., Hoffman, E.A., 2012. Assessment of morphometry of pulmonary acini in mouse lungs by nondestructive imaging using multiscale microcomputed tomography. Proc. Natl. Acad. Sci. 109 (42), 17105–17110.

Wang, S.M., Inthavong, K., Wen, J., Tu, J.Y., Xue, C.L., 2009. Comparison of micron-and nanoparticle deposition patterns in a realistic human nasal cavity. Respir. Physiol. Neurobiol. 166 (3), 142–151.

Weibel, E., 1963. Morphometry of the Human Lung. Academic Press, New York.

Winkler-Heil, R., Hofmann, W., 2016. Modeling particle deposition in the Balb/c mouse respiratory tract. Inhal. Toxicol. 28 (4), 180–191.

Wolff, R.K., 2015. Toxicology studies for inhaled and nasal delivery. Mol. Pharm. 12 (8), 2688–2696.

Xi, J., Kim, J., Si, X.A., Corley, R.A., Zhou, Y., 2016. Modeling of inertial deposition in scaled models of rat and human nasal airways: towards in vitro regional dosimetry in small animals. J. Aerosol Sci. 99, 78–93.

Yeh, H., Schum, G.M., 1980. Models of human lung airways and their application to inhaled particle deposition. Bull. Math. Biol. 42 (3), 461–480.

Yu, C.P., Diu, C.K., 1982. A comparative study of aerosol deposition in different lung models. Am. Ind. Hyg. Assoc. J. 43 (1), 54–65.

Zamankhan, P., Ahmadi, G., Wang, Z., Hopke, P.K., Cheng, Y., Su, W.C., Leonard, D., 2006. Airflow and deposition of nano-particles in a human nasal cavity. Aerosol Sci. Technol. 40 (6), 463–476.

Zhang, Z., Kleinstreuer, C., 2011. Laminar-to-turbulent fluid–nanoparticle dynamics simulations: model comparisons and nanoparticle-deposition applications. Int. J. Numer. Method. Biomed. Eng. 27 (12), 1930–1950.

Zhang, Z., Kleinstreuer, C., Kim, C.S., 2008. Airflow and nanoparticle deposition in a 16-generation tracheobronchial airway model. Ann. Biomed. Eng. 36 (12), 2095–2110.